Contribution of the lower atmosphere to the day-to-day variation of thermospheric density

Jia Yue[1,2], Wandi Yu[3], Nick Pedatella[4], Sean Bruinsma[5], Ningchao Wang[6], Huixin Liu[7]

1. NASA GSFC, 8800 Greenbelt Rd, Greenbelt, MD, 20771 USA
2. Catholic University of America, 620 Michigan Ave., N.E., DC, 20064 USA
3. Hampton University, 100 E. Queen St, Hampton, VA, 23669 USA
4. NCAR High Altitude Observatory, 3090 Center Green Drive, Boulder, CO, 80301 USA
5. OMP/GET-CNES, Space Geodesy Office, 18 avenue Edouard Belin 31 401 TOULOUSE CEDEX 4 FRANCE
6. NASA Langley Research Center, 1 NASA Dr, Hampton, VA, 23666 USA
7. Kyushu University, Department of Earth and Planetary Science, 744 Motooka Nishi-ku Fukuoka 819-0395 Japan

Corresponding author: Jia Yue

Emails: Jia Yue: jia.yue@nasa.gov

Wandi Yu: WANDI.YU@HAMPTONU.EDU

Nick Pedatella: nickp@ucar.edu

Sean Bruinsma: Sean.Bruinsma@cnes.fr

Ningchao Wang: NINGCHAO.WANG@HAMPTONU.EDU

Huixin Liu: liu.huixin.295@m.kyushu-u.ac.jp

Abstract: In this paper we carried out a numerical experiment using the Specified Dynamics mode of the Whole Atmosphere Community Climate Model with thermosphere and ionosphere eXtension (SD-WACCM-X). One SD-WACCM-X run was with realistic Kp and F10.7 and the other with constant Kp and F10.7. By comparing the day-to-day variability of thermosphere mass density at 300 km (low earth orbit, LEO) and 120 km (reentry level) in these two runs, we find that the density variation at 300 km is mainly driven by geomagnetic and solar forcing while at 120 km it is exclusively controlled by the lower atmosphere. At LEO altitudes, during solar minimum and geomagnetic quiet days, the impact from the lower atmosphere is much smaller than the effect of solar and geomagnetic variations but is not negligible (5-10% vs 20%).

1. Introduction

Satellites in low Earth orbit (LEO; altitude from 250-1000 km) are constantly affected by atmospheric drag. Understanding and prediction of the drag is critical for, e.g., mission lifetime planning, reentry control or prediction, and conjunction analysis and collision avoidance The atmospheric drag is proportional to the thermospheric mass density, the relative velocity between the satellite and the co-rotating atmosphere plus winds, its surface area perpendicular to the relative velocity, its mass, and the aerodynamics coefficient (Vallado and McClain, 2001). It has been an ongoing effort to characterize and model how thermospheric mass density variations may impact satellite drag and LEO satellite orbits and understand the corresponding errors in orbit prediction (e.g., Marcos et al., 2003; McLaughlin, 2005; Storz et al., 2005; Anderson et al., 2009; Leonard et al., 2012; Emmert et al., 2017; He et al., 2020). Most recently, SpaceX lost 38 Starlink satellites during the February 3 2022 launch, likely due to a minor geomagnetic storm impact on thermosphere density and satellite drag near 210 km altitude (Hapgood et al., 2022). This underscores the significance of understanding the LEO environment on the space industry.

Empirical or semiempirical thermosphere models have been widely utilized in orbit determination for their efficiency and ease of use (Emmert, 2015). The following three CIRA

(COSPAR International Reference Atmospheres) empirical or semiempirical models of thermospheric density are commonly used: Naval Research Laboratory Mass Spectrometer Incoherent Scatter Radar (NRLMSIS2.0 or NRLMSIS-00), Drag Temperature Model (DTM-2020 or DTM-2013) and Jacchia-Bowman (JB2008) (Picone et al., 2002, Bruinsma, 2015, 2021; Bowman et al., 2008; Emmert et al., 2020). All these empirical or semiempirical models parameterize thermospheric temperature, composition or mass density based on solar and geomagnetic indices, local times, latitudes, longitudes, and seasons. Emmert (2015) provides a detailed review of these empirical or semiempirical models.

Besides the day-to-day variability of mass density that is controlled by external geomagnetic and solar forcing, it has been recognized that the lower atmosphere can also contribute to this variability, in particular during geomagnetic quiet days (Liu et al., 2017, 2021). This variability is not considered in empirical or semiempirical models because presently an index that represents all lower atmosphere forcing is not on hand. There is still a lot to learn about the physics involved in the lower atmosphere and thermosphere coupling and how to simulate the impact correctly in first principles models (Liu, 2016). Unlike the thermosphere that is subject to forcing from above and below, the lower atmosphere can be considered an internal chaotic system. So far, there has been no work to quantify how much the lower atmosphere may impact the day-to-day variability of the thermospheric density.

The lower atmosphere can affect the thermosphere mass density in many ways at different spatial and temporal scales as reviewed by Liu et al. (2017). For example, atmospheric gravity waves from the lower atmosphere and their higher order waves can propagate into the thermosphere and induce Traveling Atmospheric Disturbances (TADs) of a few hundred to thousand kilometers scale (Park et al., 2014; Forbes et al., 2016; Vadas et al., 2019; Xu et al., 2021). Because these disturbances are often transient and localized, it is unclear what the cumulative effect could be on satellite drag and orbits. On the other hand, gravity wave forcing dissipated in the lower thermosphere induces a winter-to-summer residual circulation at 100-120 km (Qian and Yue, 2017; Qian et al., 2017). This circulation reduces O/N_2 in winter and increases O/N_2 in summer. When fast primary gravity waves and their secondary or tertiary waves dissipate in the thermosphere, the body force generates more circulation cells that strongly impact the thermosphere density (Vadas and Liu, 2013). Because gravity wave excitations in the troposphere and stratosphere and propagation through the background wind have strong day-to-day variability, it is expected that the gravity wave driven circulations can also contribute to the variation of the mass density. Thermal tides excited by solar radiation and latent heating in the troposphere can penetrate into the thermosphere and cause longitudinal and local time variations (Liu et al., 2009). Leonard et al. (2012) demonstrated that the tides can significantly impact satellite orbits and reentry. Driven by terdiurnal tides from the lower thermosphere, the midnight density maximum (MDM) forms a 30% higher density around midnight (Akmaev et al., 2010). The MSIS model series have already included longitude and local time variation and captured the migrating tides (Emmert et al., 2020). When tides dissipate in the lower thermosphere, they induce enhanced mixing and alter the mass density (Yamazaki and Richmond, 2013). Traveling planetary waves such as the quasi-two-day wave (Q2DW) and quasi-6-day wave (Q6DW) and their dissipation can also directly modulate composition (O/N_2) and introduce day-to-day and longitudinal mass density variation (Yue and Wang, 2014; Gan et al., 2015; Yue et al., 2021). Those effects have not been considered or parameterized in any empirical or semiempirical models. On longer time scales (tens of days), stratosphere sudden warmings (SSWs), a stratospheric phenomenon, alter the propagations of tides and planetary waves in the upper atmosphere and dramatically change the thermospheric mass densities (Liu et al., 2011, 2013; Yamazaki et al., 2015). Liu (2016) revealed that multiple year oscillations can also exist in the thermospheric density that are related to El Niño-Southern Oscillation (ENSO) and stratospheric quasi-biennial oscillation (QBO). Because the physics behind those oscillations and variations in the thermosphere (SSW, ENSO, QBO) are still to be explored, they are not ready to be implemented in operations. Overall, the coupling between the lower atmosphere and thermosphere is a very complex and nonlinear system crossing a large range of temporal and spatial scales.

In this paper, we aim to quantify the contribution of the lower atmosphere forcing to the day-to-day variability of thermosphere density at different heights. The Whole Atmosphere Community Climate Model with thermosphere and ionosphere eXtension (WACCM-X) with a self-resolving lower atmosphere is utilized in this numerical experiment.

2. WACCM-X and numerical experiment

Whole Atmosphere Community Climate Model is one of the atmosphere components of the National Center for Atmospheric Research (NCAR) Community Earth System Model (CESM, http://www.cesm.ucar.edu) that is self-consistent and 3-D. The version of WACCM-X used in the present study has a resolution of 1.9°×2.5° latitude×longitude. The vertical resolution is 0.25 scale heights above 0.96 hPa, with a higher resolution at lower altitudes. WACCM-X has its top boundary in the upper thermosphere (4.1×10^{-7} Pa, or ~600 km). As in the regular configuration of WACCM, the chemistry module is interactive with dynamical transport and exothermic heating (Kinnison et al., 2007). Photochemistry associated with ion species (O^+, NO^+, O, N, N^+, and metastable O^+ states) is part of the chemistry package. The recent versions 2.0 and 2.1 of WACCM-X (Liu et al., 2018; Pedatella et al., 2020) utilize a self-consistent ionosphere module for WACCM-X that simulates the electron and ion temperatures, interactive electrodynamics, including wind dynamo, and O+ transport in the *F*-region. The ion drag and Joule heating are calculated according to Roble et al. (1982) with specifications of the electric field. At middle to low latitudes, the electric field is calculated self-consistently considering forcing by the wind dynamo. The solar extreme-ultraviolet (EUV) variability in WACCM-X is represented by the Solomon and Qian (2005) scheme. Ionization and dissociation rates including photoelectron effects are parameterized as a function of F10.7, height, and solar zenith angle (SZA). The high-latitude electric potential and ion convection patterns are specified according to either Heelis et al. (1982) (parameterized by 3-hourly K_p) or Weimer (2005) (with 5-min interplanetary magnetic field and solar wind conditions as inputs). The runs in the paper were performed using Heelis. The ionization rate, particle precipitation over polar cap and cusp region and Joule heating due to aurora are calculated using an analytical auroral model of Roble and Ridley (1987). The primary difference between Versions 2.0 and 2.1 is the implementation of a ramp-down in eddy diffusion coefficient with altitude above the turbopause ~100 km altitude in version 2.1. Details can be found in https://www2.hao.ucar.edu/sites/default/files/users/whawkins/WxReleaseNotes2.1.pdf. The reduced eddy diffusion leads to an increase in the O/N_2 ratio in the thermosphere and electron density in the ionosphere, resulting in a better agreement with observations. Validation of WACCM-X shows good agreement with ionosphere-thermosphere observations, including the empirical climatology, short-term variability, and during solar flares and geomagnetically disturbed periods (Liu, et al., 2018; Liu J., et al., 2018). WACCM-X used in this study is with the specific dynamics (SD-WACCM-X) whose temperature, surface pressure and winds are constrained with Modern-Era Retrospective Analysis for Research and Application (MERRA2, Gelaro et al., 2017) below 50 km. Above 60 km, the model is free running. The lower atmosphere forcing is more realistic in SD-WACCM-X. Using SD-WACCM-X also ensures that the lower atmosphere is the same in two simulations. If the simulations were free running, they would diverge, so it would be difficult to compare for a year.

We treat the lower atmosphere forcing as a "blackbox" in this study. Lower atmosphere physics self-resolved in WACCM-X that could affect the day-to-day variability of the thermosphere and validations are summarized in Liu et al. (2014). All simulated waves including tides and planetary waves show strong day-to-day variability in the mesosphere and thermosphere. Note that SD-WACCM-X is only constrained by reanalysis up to 50 km, its mesosphere and thermosphere can diverge from the observations in the Mesosphere and lower Thermosphere (MLT) (Pedatella et al., 2014). It is still meaningful to employ SD-WACCM-X to do a statistical study of the lower atmosphere impact.

Two SD-WACCM-X runs near a solar minimum of year 2019 were performed, one with the constant Kp=2 and F10.7=70 values (defined as the reference run) and another with realistic 3-hourly Kp and F10.7 (defined as the full run). By comparing the mass density between the two runs, we can derive the quantitative contributions of the lower atmosphere and solar and geomagnetic forcing in WACCM-X. This is like the numerical work done two decades ago by Mendillo et al. (2002). They employed a coupled Thermosphere Ionosphere Mesosphere and Electrodynanics General Circulation Model/Climate Community Model version 3 (TIME-GCM-CCM3) (the predecessor to WACCM-X at NCAR) to quantify the influence of meteorological disturbances on the ionosphere by holding solar and geomagnetic conditions at constant levels. The current work is timely using a whole atmosphere model. It can also shed light on the day-to-day variability of the ionosphere as well since the thermosphere and ionosphere are closely coupled and interactive. A pioneering work by Fang et al. (2018) took a similar approach using the Whole Atmosphere Model-Global Ionosphere Plasmasphere (WAM-GIP) during June and July 2012. They performed simulations to delineate the impact of solar, magnetosphere and lower atmosphere forcing on the variability of different ionosphere parameters such as NmF2 and TEC. Thermospheric parameters such as O/N2, temperature and winds are also compared between all variability run and lower atmosphere variability run.

3. Results

3.1 LEO orbits

In this paper, we focus on two altitudes, 300 km representing the LEO orbital altitude and 120 km representing the reentry level. Daytime and nighttime densities are selected at 2 AM and 2 PM local time. To "emulate" the accumulative effect of air mass density that satellites fly through in polar LEO, we integrated the density along the meridian line from 90°S to 90°N at longitude 0°. Figure 1a shows the daily mass density at 300 km in the full run with realistic Kp and F10.7 being illustrated in Figure 2. The daytime density is greater than the nighttime density due to the diurnal solar heating and thermal expansion/contraction. To remove the well-known annual oscillation (AO) and semi-annual oscillation (SAO) and isolate the day-to-day variability, we calculated the 60-day running mean mass density in Figure 1b. AO (the June solstice density smaller than the December solstice) and SAO (densities during equinoxes are larger than solstices) are in good agreement with past observations (e.g., Jacchia, 1965; Bowman et al., 2008a; Yue et al., 2019). In addition to the "thermospheric spoon effect" that is driven by the thermosphere circulation (Fuller-Rowell, 1998), the lower atmosphere forcing such as gravity wave associated eddy diffusion could also contribute to the formation of AO and SAO (Qian et al., 2009). The day-to-day variation of the mass density is highlighted by calculating residuals shown in Figure 1c. The residual density is calculated by subtracting the 60-day running mean density (Figure 1b) from the total density (Figure 1a). The relative day-to-day variability in both day and night is similar, on the scale of ~20 %. Because Kp and F10.7 in Figure 2 are highly correlated to density variation in Figure 1, it is obvious that these short-term density variations are primarily driven by geomagnetic activities (Joule heating and particle precipitation) and solar EUV.

For comparison, Figure 3 shows the results from the SD-WACCM-X run with constant Kp and F10.7. The differences are distinct: the day-to-day variability of the mass density is substantially smaller in the run with constant Kp and F10.7. Interestingly AO and SAO in the 60-day running mean (Figure 3b) are almost identical to the full run (Figure 1b). Since the upper atmosphere energy input is reduced with on average smaller Kp, the overall mass density is smaller. The residual day-to-day variability of the density is only ~5-10% in Figure 3c. This variability is exclusively caused by the lower atmosphere impact. The daytime/nighttime difference in the variability is likely caused by the day-to-day variation of tides. Comparing to the realistic variability of ~20%, we conclude that the day-to-day variation of mass density and satellite drag in LEO is mainly driven by geomagnetic and solar forcing. The impact from the lower atmosphere is secondary, but not negligible.

To further investigate how the day-to-day density variability at 300 km is controlled by Kp, we separate the days between quiet ($Kp<1$) and more active ($Kp\geq1$) days based on the actual Kp value. Figure 4 illustrates this difference of the mass density at 2 PM. During active days (Figure 4c), the day-to-day variability of ~20% is dominated by geomagnetic forcing comparing to ~5-10% driven by the lower atmosphere. On the other hand, when Kp is small, although geomagnetic and solar forcing are still the main drivers, the lower atmosphere forcing is not negligible. This is quantified by the statistics of the residual daily mass density in Figure 5. Comparing the first and third bar, the variability is reduced dramatically during quiet times, but it is still larger than the corresponding constant Kp/F10.7 run (second bar of Figure 5).

In this paper, we will not examine the exact physical mechanisms behind the variability of the mass density caused by geomagnetic, solar, and lower atmosphere forcing. But it is still useful to calculate the characteristics of this variability by performing the wavelet and Fast Fourier Transform (FFT) analysis, as shown in Figure 6. In the realistic Kp and F10.7 run, an oscillation with a period ~13.5 days, related to the 27-day solar rotation cycle, is prominent (Figure 6b). This is in agreement with the power spectra of Kp and F10.7 itself (Figure 2). Throughout the year multi-day oscillations show up in different periods, for example, 7-days variations from day 0-50, and 7, 9, and 12-day variations in September (Figure 6a). On the contrary in Figure 6c, the constant Kp/F10.7 run shows little oscillations except multiple day periods during equinoxes. Naturally, the 13.5-day oscillation is absent in Figure 6d.

3.2 Reentry level

The same analysis is repeated on the SD-WACCM-X mass density at 120 km, the satellite reentry level. The scenario is completely opposite to 300 km. Figures 7 and 8 show the day-to-day variability of air density at 120 km for the reference and full runs, respectively. They are nearly identical, because the geomagnetic and solar forcing has very weak impact on the density at 120 km altitude. Both the AO and SAO are well reproduced (Figure 7b and 8b). Daytime and nighttime densities are on the same scale, with slightly larger values at night. This difference comes from upward propagating tides. The day-to-day variability, which is less than 10%, is entirely driven by the lower atmosphere as aforementioned. This is further quantified in the statistics of the residual density at 120 km (Figure 9). Clearly the mass density during the active time and quiet time is similar. And the variance for the constant Kp/F10.7 run is the same as the realistic Kp/F10.7 run. Lastly, we performed the wavelet and FFT analysis, which is shown in Figure 10. Because the extreme Ultra Violet (EUV) heating takes place well above 120 km, the 13.5-day period oscillation is not present in the realistic Kp/F10.7 run. There are minor differences in the wavelet spectrum between the constant and realistic Kp runs. Geomagnetic effects can sometimes penetrate downward to the MLT region especially during days with enhanced geomagnetic activity. Then the slightly different MLT background responds differently to the same lower atmosphere waves. In conclusion, the day-to-day variability of the density at the reentry level is completely controlled by the lower atmosphere, opposite to the variability higher in the thermosphere.

3.3 Transition layer from lower atmosphere forcing to solar and geomagnetic forcing

It is also important to know where the transition height is from the lower atmosphere influenced lower thermosphere to solar and geomagnetic controlled upper thermosphere. To shed some light on the transition altitude, Figure 11 shows the statistics of the mass density at 130 km, 140 km and 150 km. Comparing the third and fourth bar, the mass density variability for realistic Kp/F10.7 run during active days increases with height relative to the constant Kp/F10.7 run. Therefore, the transition layer ranges from 130-150 km. Note that the Starlink satellites were launched to 210 km, the thermosphere density enhancement that led to strong satellite drag was mainly caused by the minor geomagnetic storm, consistent with the conclusion of Hapgood et al. (2022).

The transition layer at 130-150 km is not contradictory to the Space Atmosphere Interaction Region (SAIR) between 100 and 130 km defined by Sojka (2017). Three space weather forcings are considered in Sojka (2017): the solar photon flux (flares), particle precipitation (aurora) and electromagnetic Joule heating (magnetosphere-ionosphere coupling). At 100-130 km, their effects on the neutral density and temperature focus on auroral high latitudes and polar cap regions. On the other hand, this paper concerns the pole-to-pole latitudinally averaged neutral density, not a single location at high latitudes.

4. Discussion and Summary

This numerical experiment was carried out during a solar minimum year of 2019 when the influence of the geomagnetic and solar activities on the thermosphere were small compared to solar maximum. The ability of lower atmosphere waves to propagate into the thermosphere varies with solar activity, which may reduce the effects at solar maximum. For example, molecular diffusion and ion drag are stronger during solar maximum, thus, lower atmosphere waves experience stronger damping in the thermosphere. The conclusions could thus be vastly different during solar maximum. To gain a comprehensive understanding, a similar experiment needs to be carried out for a solar maximum year. Since storm effects on the thermosphere normally last one day, the classification of $Kp>1$ and $Kp<1$ based on 3-hourly values without time lag may introduce some uncertainties in the magnitude of variability. Thus, more rigorous analysis is required for individual storms.

There are two other whole atmosphere models in addition to WACCM-X, Ground-to-topside model of Atmosphere and Ionosphere for Aeronomy (GAIA; Miyoshi et al., 2011, 2012) and the coupled Whole Atmosphere Model-Ionosphere Plasmasphere Electrodynamics (WAM-IPE; Fuller-Rowell et al., 2020). Each has different representations of the lower atmosphere, thermosphere and ionosphere. To gain a more robust result, it will be beneficial to compare the results in this paper with the same experiment but being carried out with different whole atmosphere models.

The validity of this work solely depends on the implementation of lower atmosphere coupling with the thermosphere and ionosphere in WACCM-X. This is always an ongoing effort with the advancement of observations, theories, and algorithms. For example, secondary and higher order gravity waves excited by primary wave breaking have not been well resolved in any whole atmosphere models (Becker and Vadas, 2020). Furthermore, gravity waves still rely on parameterizations in WACCM which is just an approximation and ignores lateral propagation of waves (Garcia et al., 2017). The MLT in SD-WACCM-X also diverges from observations as it is not constrained by data (Pedatella et al., 2014). Our understanding of the lower atmosphere impact on the thermosphere density will therefore continue evolving with the ongoing development of whole atmosphere models.

This paper carried out a numerical experiment using a whole atmosphere model by comparing the day-to-day variability of thermosphere mass density at 300 km (LEO) and 120 km (reentry level). We find that the density variation at LEO is mainly driven by geomagnetic and solar forcing while at reentry altitude it is controlled by the lower atmosphere. At LEO altitudes, during solar minimum and geomagnetic quiet days, the impact from the lower atmosphere is much smaller compared to solar and geomagnetic effects, but is not negligible (5-10% vs 20%). To further quantify the impact from the lower atmosphere on satellite drag, we need to apply orbit prediction using whole atmosphere modeled density like those done in He et al. (2020).

Acknowledgement:

JY is supported by NSF 2140031 and NASA CCMC grant. H. L. acknowledges supports by JSPS KAKENHI Grants 18H01270, 17KK0095, and JRPs-LEAD with DFG program JPJSJRP 20181602. SB is supported by CNES APR grant METEOESP. NP acknowledges support from NASA Grant 80NSSC20K0628. This material is based upon work supported by the National Center for Atmospheric Research, which is a major facility sponsored by the U.S. National Science Foundation under Cooperative Agreement 1852977. We would like to acknowledge high-performance computing support from Cheyenne (doi:10.5065/D6RX99HX) provided by NCAR's Computational and Information Systems Laboratory, sponsored by the National Science Foundation. We thank the organizers of the ISWAT 2020 meeting in Florida where the initial discussions took place. We thank the constructive comments made by the two anonymous reviewers.

Appendix:

The analysis performed in Section 3.2 is to compare directly with the results at 300 km. In reality, it is impossible that a satellite can fly horizontally from pole to pole at 120 km due to overwhelmingly large satellite drag. To simulate a more realistically vertical reentry trajectory, we calculated the integrated mass density vertically from 130 km to 80 km and from 90N to 0 latitude, following Figure 10 of Leonard et al. (2012). Below ~80 km, the space object falls freely. The results are identical to the analysis at 120 km in Section 3.2. Geomagnetic and solar forcing has no control of reentry trajectory. Lower atmosphere exclusively impacts the reentry. Figures A1, A2, A3, A4 support this conclusion.

References:

Akmaev, R. A., Wu, F., Fuller-Rowell, T. J., Wang, H., Iredell, M. D., 2010. Midnight density and temperature maxima, and thermospheric dynamics in Whole Atmosphere Model simulations. J. Geophys. Res.. 115, A08326. https://doi:10.1029/2010JA015651.

Anderson, R. L., Born, G. H., Forbes, J. M., 2009. Sensitivity of orbit predictions to density variability. J. of Spacecraft and Rockets. 46, 6, 1214-1230. https://doi.org/10.2514/1.42138.

Becker, E., Vadas, S.L., 2020. Explicit global simulation of gravity waves in the thermosphere. J. Geophys. Res. Space Physics. 125, e2020JA028034. https://doi.org/10.1029/2020JA028034.

Bowman, B. R., Tobiska, W. K., Kendra, M. J., 2008a. The thermospheric semiannual density response to solar EUV heating. Journal of Atmospheric and Solar - Terrestrial Physics. 70(11-12), 1482–1496. https://doi.org/10.1016/j.jastp.2008.04.020.

Bowman, B.R., Tobiska, W.K., Marcos, F.A., Huang, C.Y., Lin, C.S., Burke, W.J., 2008b. A new empirical thermospheric density model JB2008 using new solar and geomagnetic indices. In: AIAA/AAS Astrodynamics Specialist Conference, 18–21 August 2008, Honolulu, Hawaii, paper AIAA 2008–6438.

Bruinsma, S.L., 2015. The DTM-2013 thermosphere model. J. Space Weather Space Clim. 5, A1. http://dx.doi.org/10.1051/swsc/2015001.

Bruinsma, S., Boniface, C., 2021. The operational and research DTM-2020 thermosphere models. J. Space Weather Space Clim.. 11, 47. https://doi.org/10.1051/swsc/2021032.

Emmert, J. T., 2015. Thermospheric mass density: a review. Advances in Space Research. 56, 773-824. https://doi.org/10.1016/j.asr.2015.05.038.

Emmert, J. T., Warren, H. P., Segerman, A. M., Byers, J. M., Picone, J. M., 2017. Propagation of atmospheric density errors to satellite orbits, Advances in Space Research, 59, 147-165. https://doi.org/10.1016/j.asr.2016.07.036.

Emmert, J. T., Drob, D. P., Picone, et al., 2020. NRLMSIS 2.0: A whole-atmosphere empirical model of temperature and neutral species densities. Earth and Space Science, 7, e2020EA001321. https://doi.org/10.1029/2020EA001321.

Fang, T.-W., Fuller-Rowell, T., Yudin, V., Matsuo, T., Viereck, R., 2018. Quantifying the sources of ionosphere day-to-day variability. J. Geophys. Res. Space Physics, 123, 9682-9696. https://doi.org/10.1029/2018JA025525.

Forbes, J. M., Bruinsma, S. L., Doornbos, E., Zhang, X., 2016. Gravity wave-induced variability of the middle thermosphere. J. Geophys. Res. Space Physics. 121, 6914–6923. https://doi:10.1002/2016JA022923.

Fuller-Rowell, T. J., 1998. The “thermospheric spoon”: A mechanism for the semiannual density variation. Journal of Geophysical Research. 103(A3), 3951–3956. https://doi.org/10.1029/97JA03335.

Fuller-Rowell, T., 2020. Transition of WAM-IPE to NOAA Operations: Current capabilities and future potential. AMS 2020. session 6 R2O2R.

Gan, Q., Yue, J., Chang, L.C., Wang, W.B., Zhang, S.D., Du, J., 2015. Observations of thermosphere and ionosphere changes due to the dissipative 6.5-day wave in the lower thermosphere. Annales Geophysicae. 33, 913-922. https://doi:10.5194/angeo-33-913-2015.

Garcia R. R., Smith, A. K., Kinnison, D. E., de la Camara, A., Murphy, D. J., 2017. Modification of the gravity wave parameterization in the Whole Atmosphere Community Climate Model: motivation and results. Journal of the Atmospheric Sciences. 74, 275-291. https://doi.org/10.1175/JAS-D-16-0104.1.

Gelaro, R., McCarty, W., Suárez, M. J., et al., 2017. The modern-era retrospective analysis for research and applications, version 2 (MERRA-2). Journal of Climate. **30**(14), 5419– 5454. https://doi.org/10.1175/JCLI-D-16-0758.1.

Hapgood, M., Liu, H. Lugaz, N., 2022. Space-X – Sailing close to the space weather? Space Weather. 20, e2022SW003074. https://doi.org/10.1029/2022SW003074.

He, C., Yang, Y., Carter, B., et al., 2020. Impact of thermospheric mass density on the orbit prediction of LEO satellites. Space Weather. 18, e2019SW002336. https://doi.org/10.1029/2019SW002336.

Heelis, R. A., Lowell, J. K., Spiro, R. W., 1982. A model of the high-latitude ionospheric convection pattern. Journal of Geophysical Research: Space Physics. **87**, 6339– 6345. https://doi.org/10.1029/JA087iA08p06339.

Jacchia, L. G., 1965. Static diffusion models of the upper atmosphere with empirical temperature profiles. Smithsonian Contributions to Astrophysics, 8, 215–257.

Kinnison, D. E., Brasseur, G. P., Walters, S., et al., 2007. Sensitivity of chemical tracers to meteorological parameters in the MOZART-3 chemical transport model. J. Geophys. Res.. 112 (D20), D20302. https://doi:10.1029/2006JD007879.

Leonard, J. M., Forbes, J. M., Born, G. H., 2012. Impact of tidal density variability on orbital and reentry predictions. Space Weather. 10, S12003. https://doi:10.1029/2012SW000842.

Liu H., Yamamoto, M., Lühr, H., 2009. Wave-4 pattern of the equatorial mass density anomaly- A thermospheric signature of tropical deep convection. Geophys. Res. Lett.. 36, L18104. https://doi:10.1029/2009GL039865.

Liu, H., 2016. Thermospheric inter-annual variability and its potential connection to ENSO and stratospheric QBO. Earth Planet Space. 68, 1–10. https://doi:10.1186/s40623-016-0455-8.

Liu, H., Doornbos, E., Yamamoto, M., Tulasi Ram, S., 2011. Strong thermospheric cooling during the 2009 major stratosphere warming. Geophys. Res. Lett.. 38, L12102. https://doi:10.1029/2011GL047898.

Liu, H., Jin, H., Miyoshi, Y., Fujiwara, H., Shinagawa, H., 2013. Upper atmosphere response to stratosphere sudden warming: Local time and height dependence simulated by GAIA model. Geophys. Res. Lett.. 40, 635–640. https://doi:10.1002/grl.50146.

Liu, H., Thayer, J., Zhang, Y., Lee, W. K., 2017. The non–storm time corrugated upper thermosphere: What is beyond MSIS?. Space Weather. 15, 746–760. https://doi:10.1002/2017SW001618.

Liu H., Yamazaki, Y., Lei, J., 2021. Chapter 8: Day-to-day variability of the thermosphere and ionosphere, in *Upper Atmosphere Dynamics and Energetics, AGU monography,* ed. W. Wang, Y. Zhang, ISBN: 978-1-11950-756-7.

Liu, H.-L., 2014. WACCM-X simulation of tidal and planetary wave variability in the upper atmosphere. Modeling the Ionosphere-Thermosphere System, J. Huba, R. Schunk, and G. Khazanov, Eds., Geophysical Monograph Series, American Geophysical Union, Washington, 181-200 doi:10.1002/9781118704417.ch16.

Liu, H.-L., 2016. Variability and predictability of the space environment as related to lower atmosphere forcing. Space Weather. 14, 9, 2016SW001450. https://doi:10.1002/2016SW001450.

Liu, H.-L., Bardeen, C. G., Foster, B. T., et al., 2018. Development and validation of the Whole Atmosphere Community Climate Model with thermosphere and ionosphere extension (WACCM-X 2.0). Journal of Advances in Modeling Earth Systems. 10, 381–402. https://doi.org/10.1002/.

Liu, J., Liu, H., Wang, W., et al., 2018. First results from the ionospheric extension of WACCM-X during the deep solar minimum year of 2008. Journal of Geophysical Research: Space Physics. 123,1534–1553. https://doi.org/10.1002/2017JA025010.

Marcos, F. O., Wise, J. O., Kendra, M. J., Grossbard, N. J., 2003. Satellite drag research: Past, present, and future. Adv. Astronaut. Sci.. 116, 1865–1878.

Mendillo, M., Rishbeth, H., Roble, R. G., Wroten, J., 2002. Modeling F2-layer seasonal trends and day-to-day variability driven by coupling with the lower atmosphere. JASTP. 64, 1911-1931. https://doi.org/10.1016/S1364-6826(02)00193-1.

McLaughlin, C. A., 2005. Upper atmospheric phenomena and satellite drag. Adv. Astronaut. Sci.. 123, 989–996.

Miyoshi, Y., Fujiwara, H., Jin, H., Shinagawa, H., Liu, H., 2012. Numerical simulation of the equatorial wind jet in the thermosphere. J. Geophys. Res.. 117, A03309. https://doi:10.1029/2011JA017373.

Miyoshi, Y., Fujiwara, H., Jin, H., Shinagawa, H., Liu, H., Terada, K., 2011. Numerical Simulation of the Equatorial Mass Density Anomaly. Journal of Geophysical Research. 116, A05322. https://doi:10.1029/2010JA016315.

Park, J., Lühr, H., Lee, C., Kim, Y. H., Jee, G., Kim, J.-H., 2014. A climatology of medium-scale gravity wave activity in the midlatitude/low-latitude daytime upper thermosphere as observed by CHAMP. J. Geophys. Res. Space Physics. 119, 2187–2196. https://doi:10.1002/2013JA019705.

Pedatella, N. M., Raeder, K., Anderson, J. L., Liu, H.-L., 2014. Ensemble data assimilation in the Whole Atmosphere Community Climate Model. J. Geophys. Res. Atmos.. 119, 9793–9809. http://doi:10.1002/2014JD021776.

Pedatella, N. M., Anderson, J. L., Chen, C. H., Raeder, K., Liu, J., Liu, H.-L., Lin, C. H., 2020. Assimilation of Ionosphere Observations in the Whole Atmosphere Community Climate Model with Thermosphere-Ionosphere EXtension (WACCMX). Journal of Geophysical Research: Space Physics. 125, 9. https://doi:10.1029/2020JA028251.

Picone, J.M., Hedin, A.E., Drob, D.P., Aikin, A.C., 2002. NRLMSISE-00 empirical model of the atmosphere: statistical comparisons and scientific issues. J. Geophys. Res. 107, A12. http://dx.doi.org/10.1029/2002JA009430.

Qian, L., Solomon, S. C., Kane, T. J., 2009. Seasonal variation of thermospheric density and composition. Journal of Geophysical Research. 114, A01312. https://doi.org/10.1029/2008JA013643.

Qian, L., Yue, J., 2017. Impact of the lower thermospheric winter-to-summer residual circulation on thermospheric composition. Geophys. Res. Lett.. 44, 3971-3979. http://*doi:*10.1002/2017GL073361.

Qian, L., Burns, A., Yue, J., 2017. Evidence of the lower thermospheric winter-to-summer circulation from SABER CO_2 observation. Geophysical Research Letters. 44, 10100-10107. *https://*doi.org/10.1002/2017GL075643.

Roble, R. G., Ridley, E.C., Dickinson, R. E., 1982. Global circulation and temperature structure of the thermosphere with high-latitude convection. J. Geophys. Res.. 87, 1599-161. https://doi.org/10.1029/JA087iA03p01599.

Roble, R. G., Ridley, E. C., 1987. An auroral model for the ncar thermosphere general circulation model (TGCM). Annales Geophysicae. **5A**, 369– 382.

Sojka, J. J., 2017. Locations where space weather energy impacts the atmosphere. Space Sci. Rev., 212:1041-1067. Doi: 10.1007/s11214-017-0379-z.

Solomon, S. C., Qian, L., 2005. Solar extreme-ultraviolet irradiance for general circulation models. J. Geophys. Res. 110, A10306. Doi: 10.1029/2005JA011160.

Storz, M. F., Bowman, B. R., Branson, M. J., Casali, S. J., Tobiska, W. K., 2005. High accuracy satellite drag model (HASDM). Advances in Space Research. 36, 2497-2505. https://doi.org/10.1016/j.asr.2004.02.020.

Vadas, S. L., Liu, H.-L., 2013. Numerical modeling of the large-scale neutral and plasma responses to the body forces created by the dissipation of gravity waves from 6 h of deep convection in Brazil, J. Geophys. Res. Space Physics. 118, 2593–2617. https://doi:10.1002/jgra.50249.

Vadas, S. L., Xu, S., Yue, J., Bossert, K., Becker, E., Baumgarten, G., 2019. Characteristics of the quiet time hot spot gravity waves observed by GOCE over the Southern Andes on 5 July 2010. Journal of Geophysical Research: Space Physics. 124, 7034–7061. https:// doi.org/10.1029/2019JA026693.

Vallado, D. A., McClain,W. D., 2001. Fundamentals of astrodynamics and applications (Vol. 12): Springer Science and Business Media.

Weimer, D. R., 2005. Improved ionospheric electrodynamic models and application to calculating joule heating rates. Journal of Geophysical Research: Space Physics. 110, A05306. https://doi.org/10.1029/2004JA010884.

Xu, S., Vadas, S. L., Yue, J., 2021. Thermospheric traveling atmospheric disturbances in austral winter from GOCE and CHAMP. Journal of Geophysical Research: Space Physics. 126, e2021JA029335. https://doi.org/10.1029/2021JA029335.

Yamazaki, Y., Richmond, A. D., 2013. A theory of ionospheric response to upward-propagating tides: Electrodynamic effects and tidal mixing effects. J. Geophys. Res. Space Physics. 118, 5891–5905. https://doi:10.1002/jgra.50487.

Yamazaki, Y., Kosch, M. J., Emmert, J. T., 2015. Evidence for stratospheric sudden warming effectson the upper thermosphere derived from satellite orbital decay data during 1967–2013. Geophys.Res. Lett.. 42, 6180–6188. https://doi:10.1002/2015GL065395.

Yue J., Wang, W. 2014. Changes of thermospheric composition and ionospheric density caused by quasi 2 day wave dissipation. *J.* Geophys. Res. Space Physics. 119, 2069-2078. https://doi:10.1002/2013JA019725.

Yue, J., Jian, Y., Wang, W., et al., 2019. Annual and semiannual oscillations of thermospheric composition in TIMED/GUVI limb measurements. Journal of Geophysical Research: Space Physics. 124, 3067–3082. https://doi. org/10.1029/2019JA026544.

Yue J., Lieberman, R., Chang, L., 2021. Planetary waves and their impact on the mesosphere, thermosphere, and ionosphere. Space Physics and Aeronomy Collection Volume 4: Upper

Atmosphere Dynamics and Energetics, Geophysical Monograph 261, ch. 10, DOI: 10.1002/9781119815631.ch10, published by Wiley, Hoboken, NJ, USA.

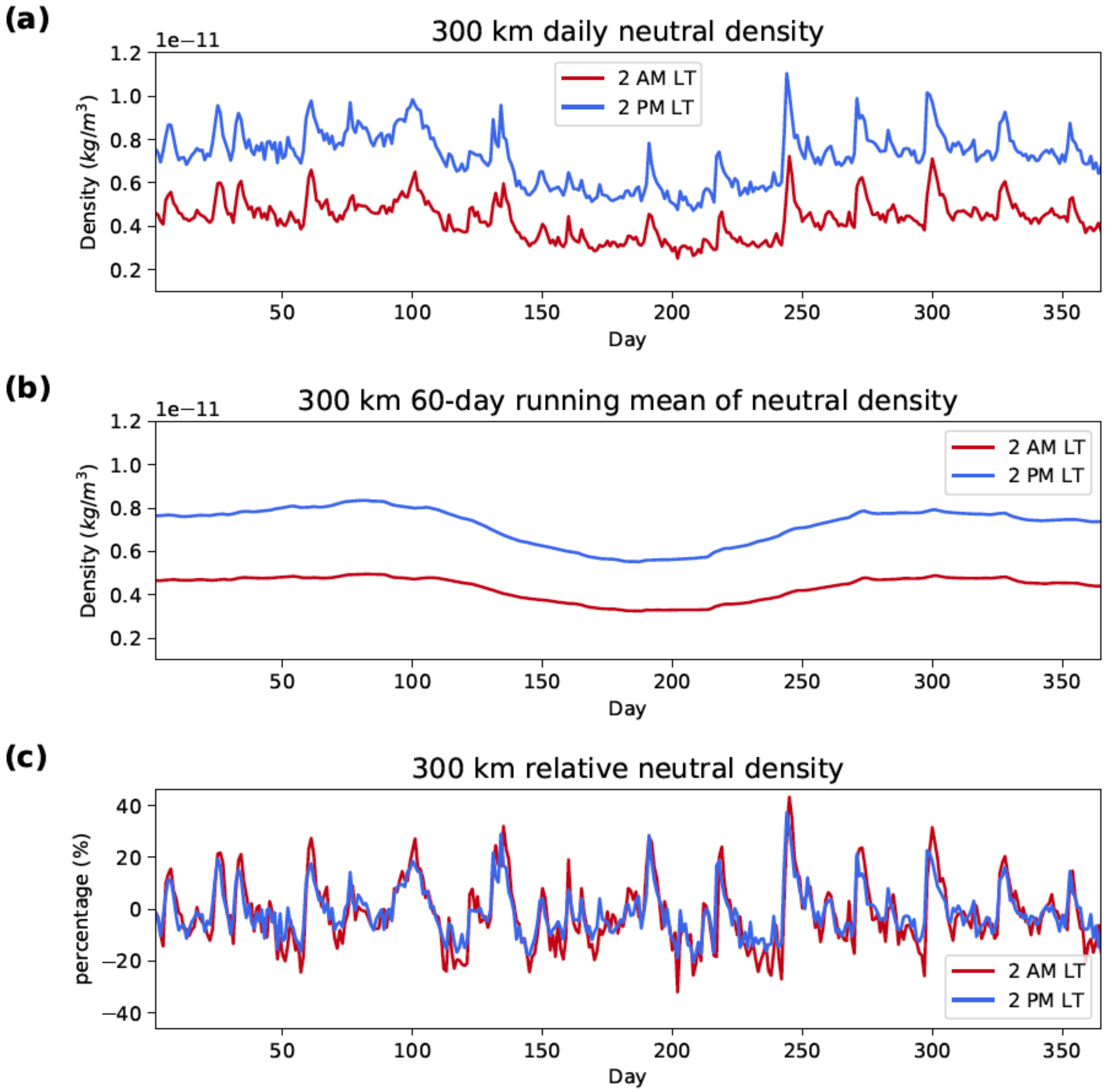

Figure 1. (a) Daily latitudinally averaged mass density at 300 km at 2 AM (red) and 2 PM (blue) local time in 2019. (b) 60-day running mean of neutral density at 300 km. (c) residual density in percentage by calculating (daily density-60-day mean density)/daily density.

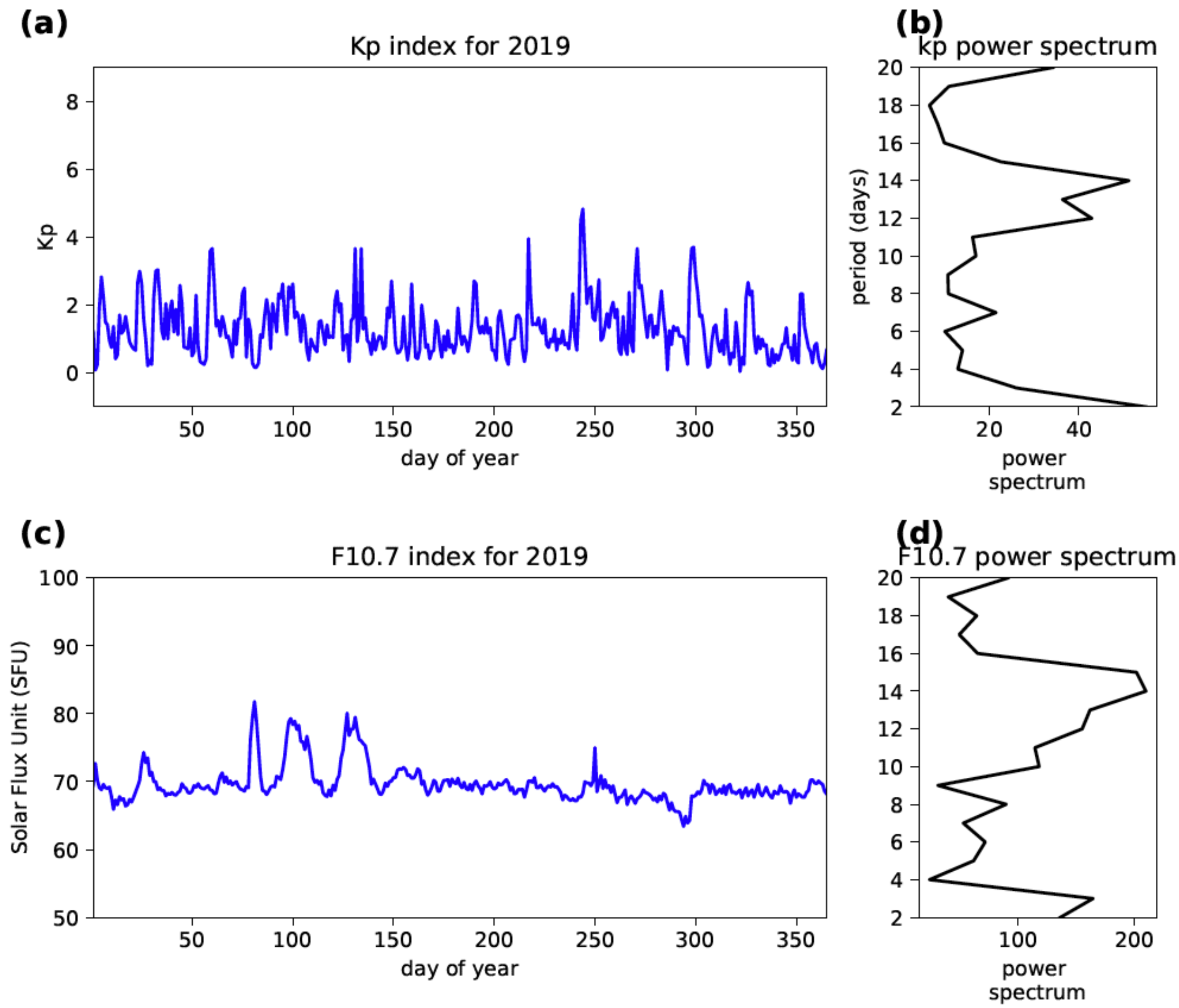

Figure 2. Daily Kp index and F10.7 index in 2019 and their power spectra.

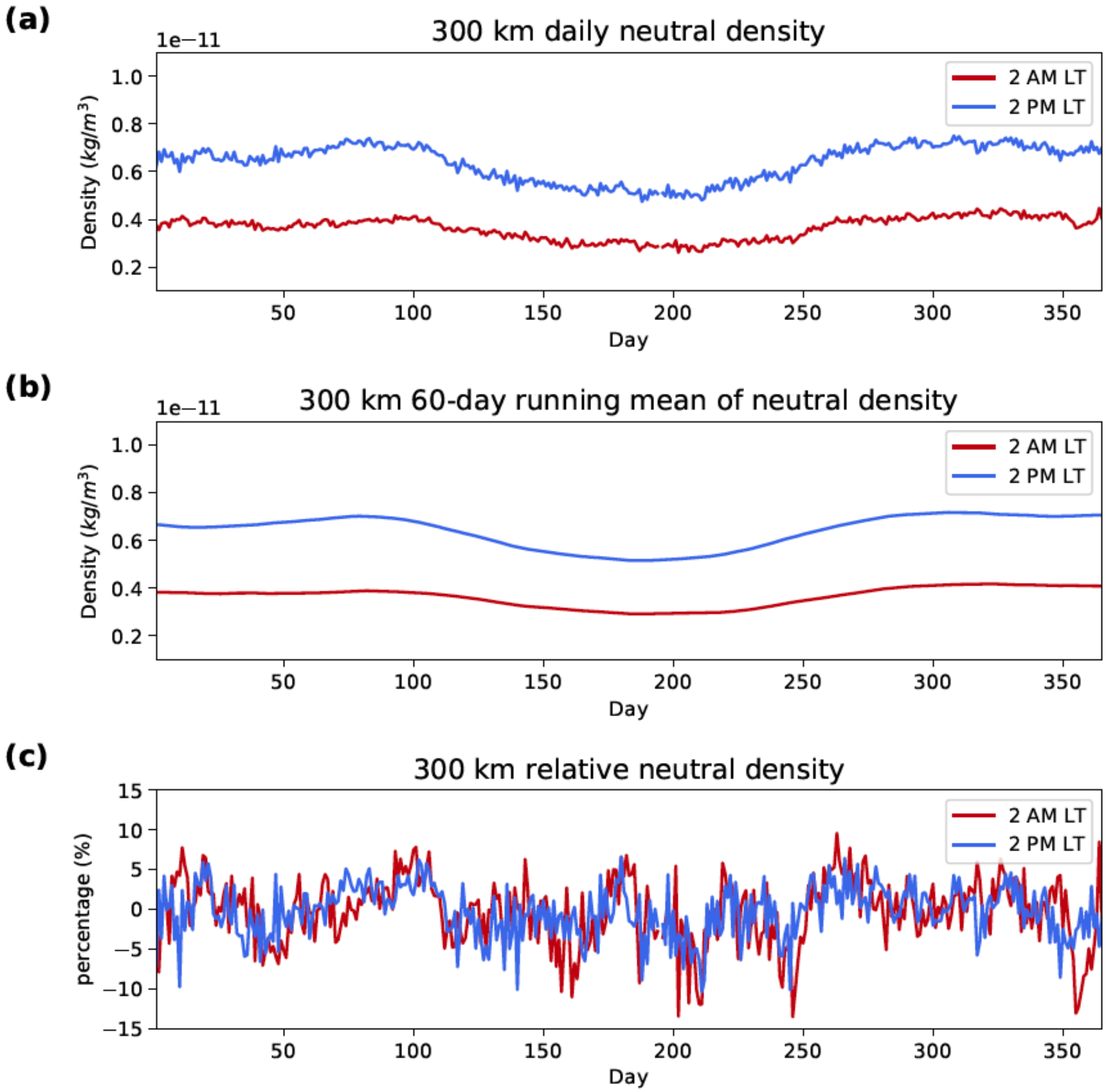

Figure 3. Similar to Figure 1, but with constant Kp=2 and F10.7=70 SFU.

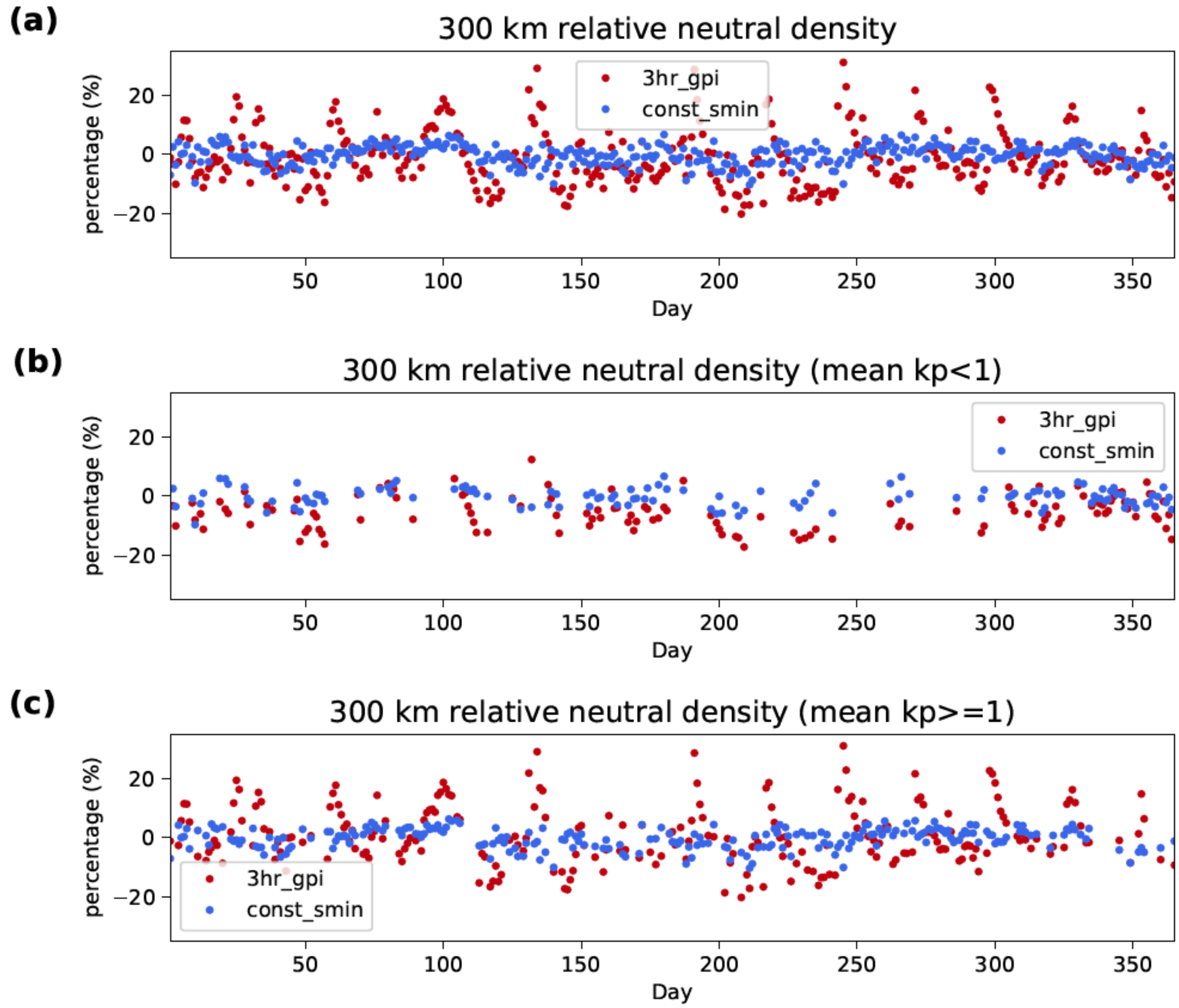

Figure 4. relative variability at 300 km from the full Kp/F10.7 run (red) and constant Kp/F10.7 run (blue). (a) all days (b) quiet day (Kp<1) (c) active day (Kp≥1).

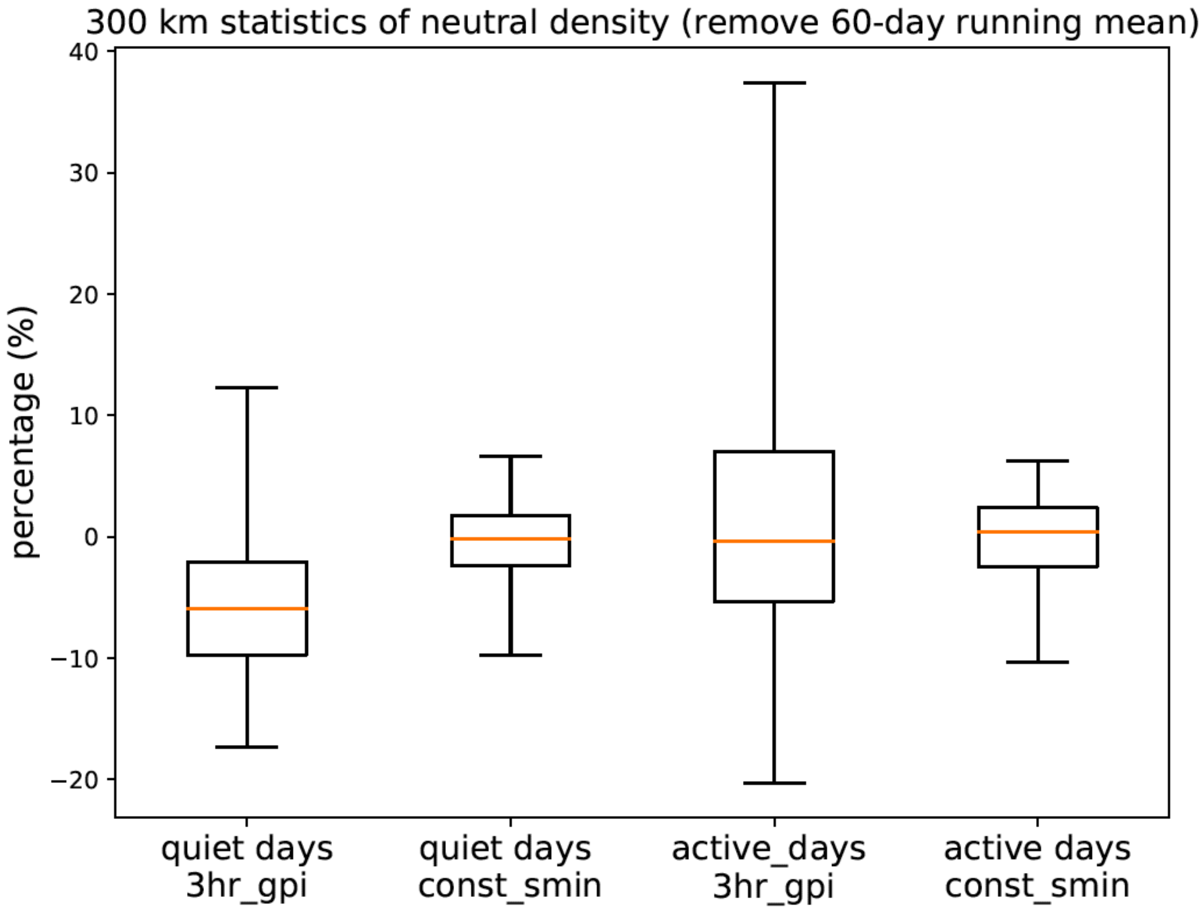

Figure 5. Statistics of residual mass density in Figure 4. From left to right: quiet days from the full Kp run, quiet days from the reference (constant Kp) run, active days from the full Kp run, and active days from the reference run. The lower and upper boundary of the box are the 25th and 75th percentiles, and the orange line is the median. The lower and upper fence are the min and max values.

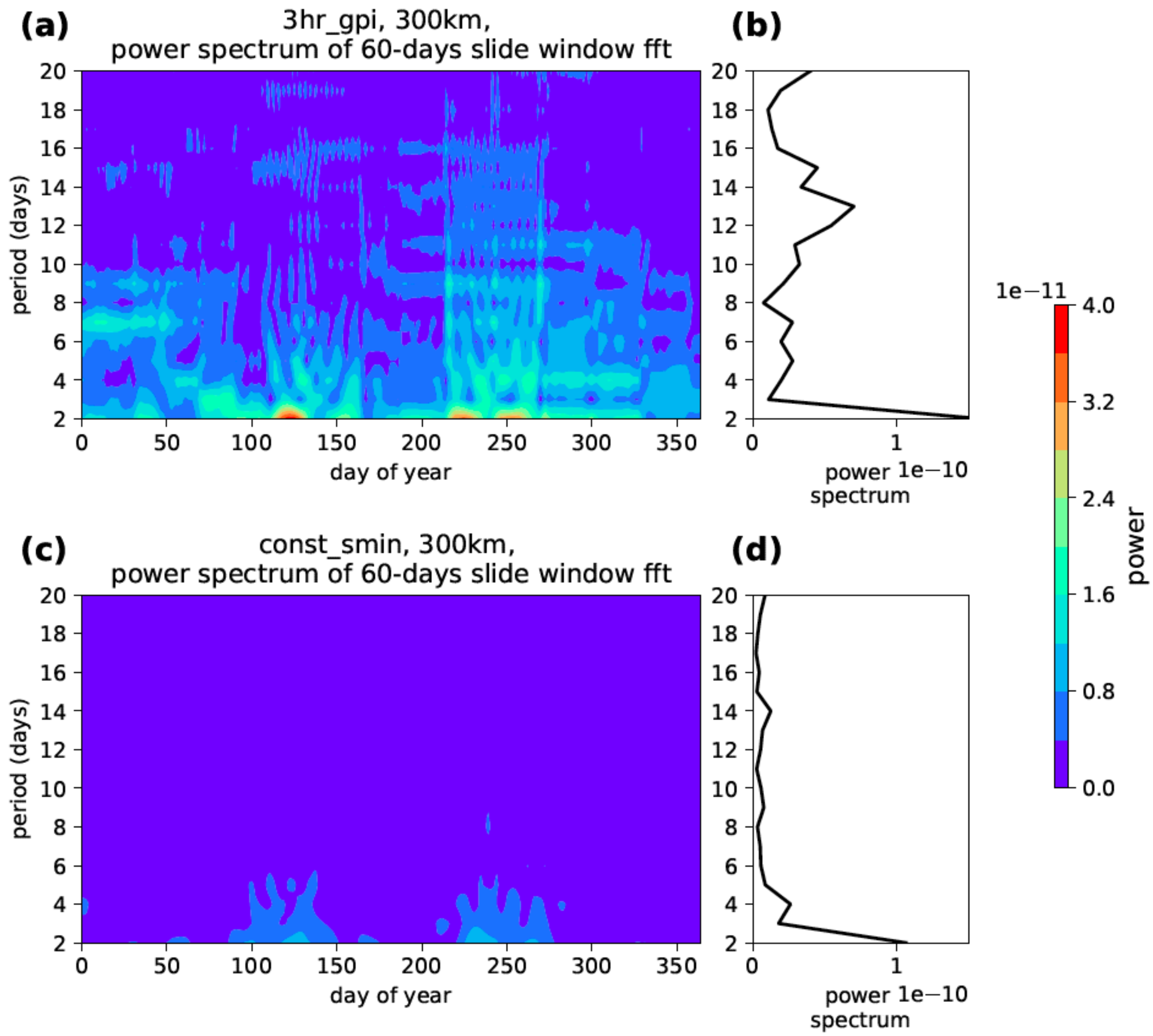

Figure 6. Wavelet (left) and FFT (right) analysis of the mass density in the realistic Kp/F10.7 run (top) and constant Kp/F10.7 run (bottom).

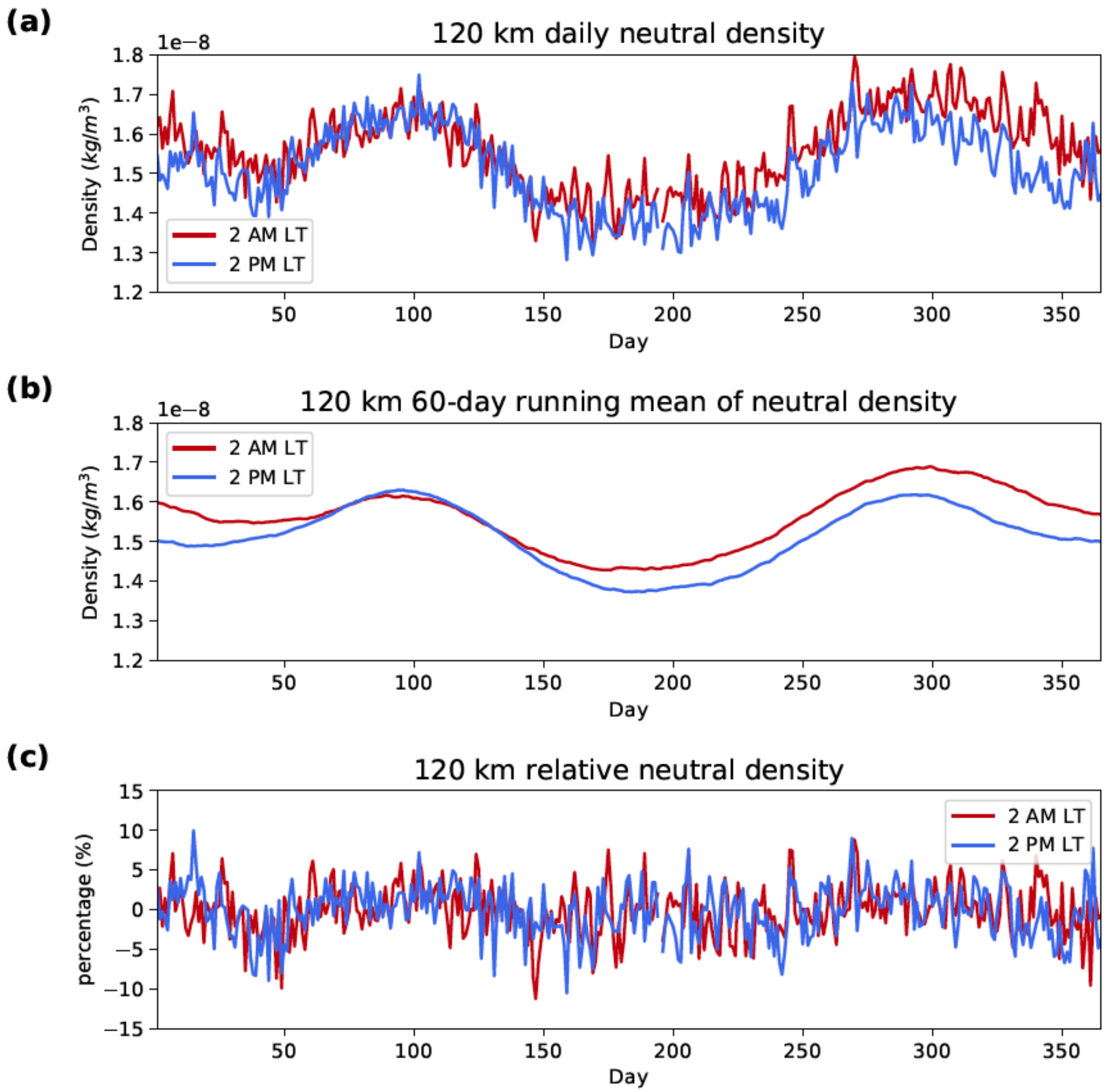

Figure 7. Similar to Figure 1 at 120 km.

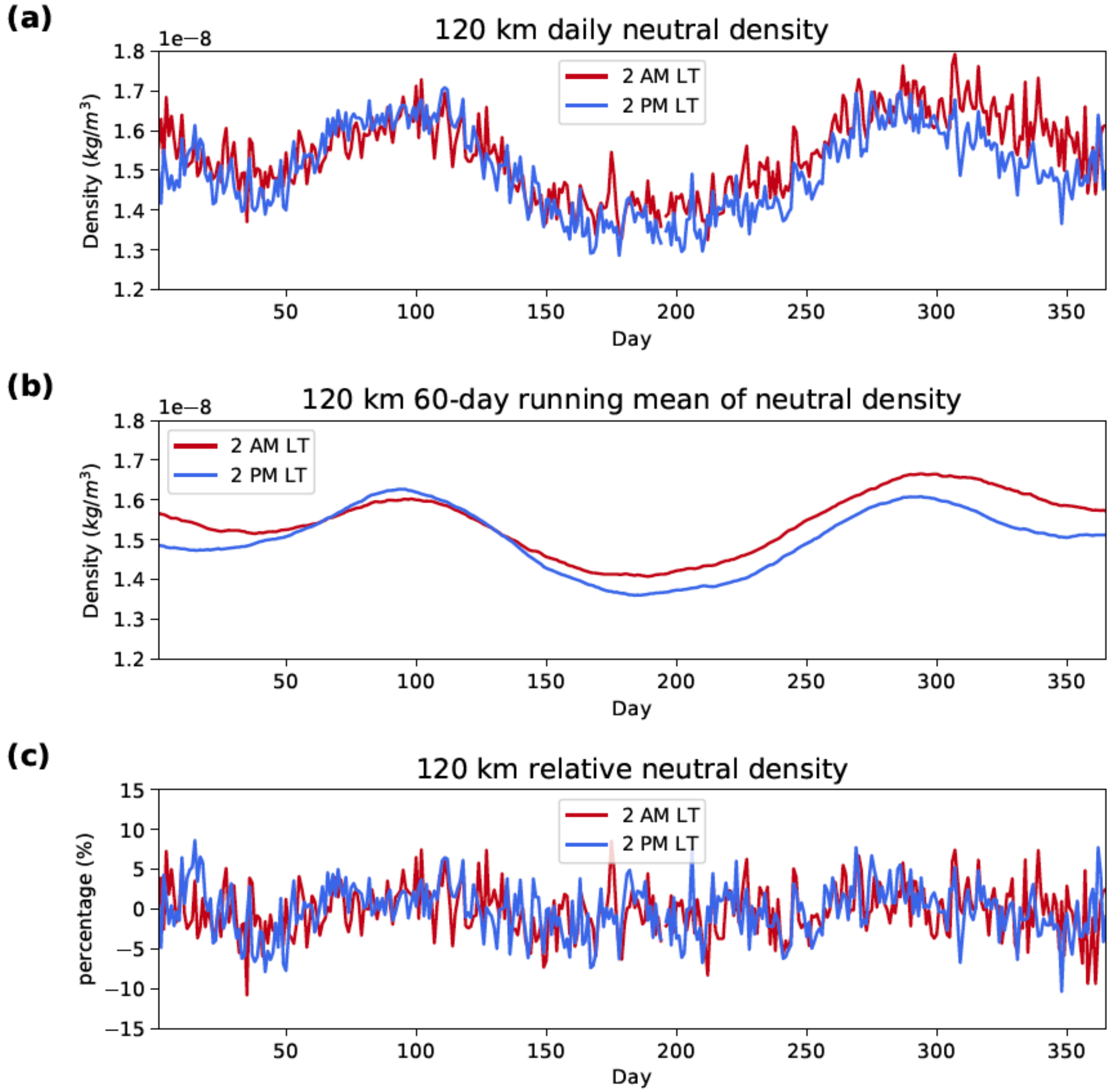

Figure 8. Similar to Figure 3 but at 120 km.

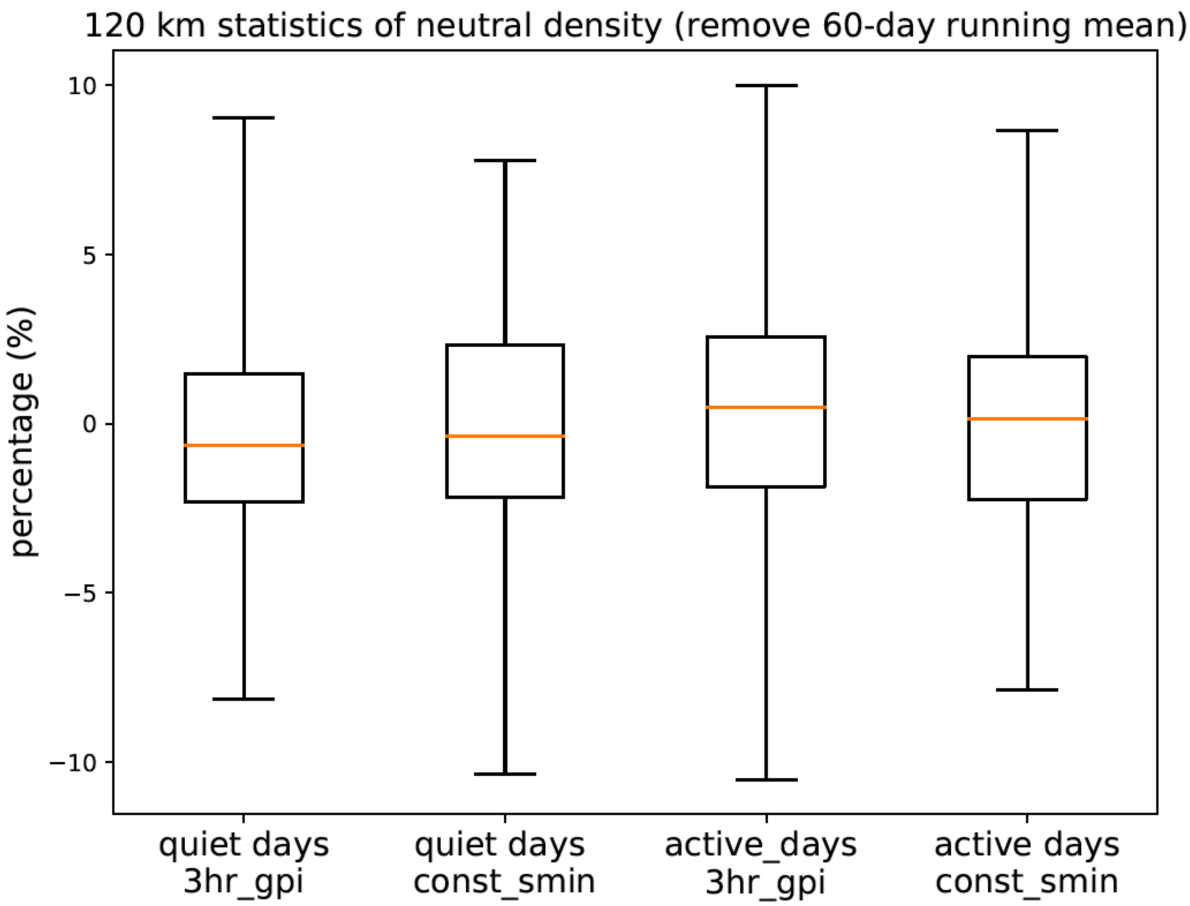

Figure 9. Similar to Figure 5 at 120 km.

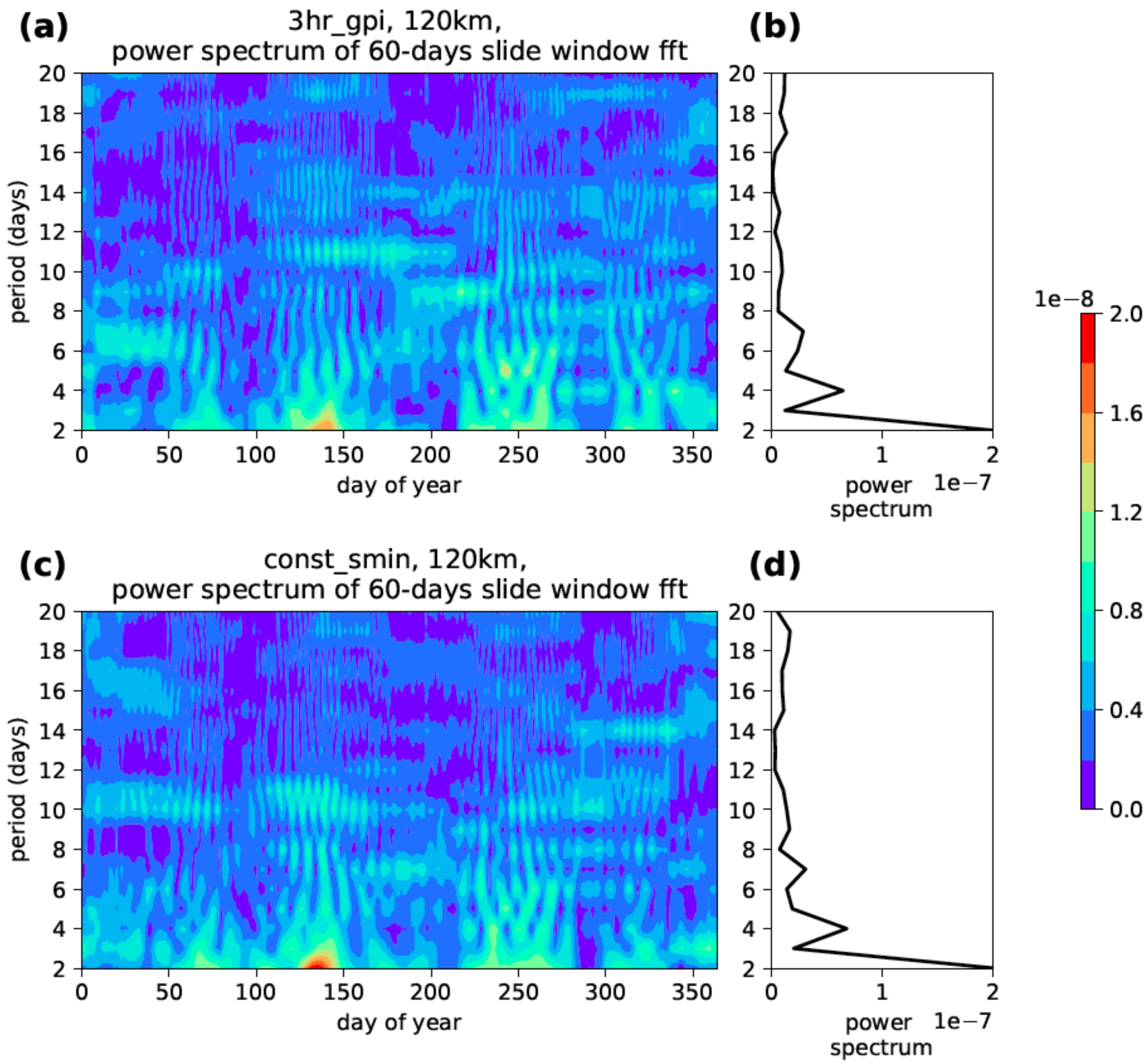

Figure 10. Similar to Figure 6 but at 120 km.

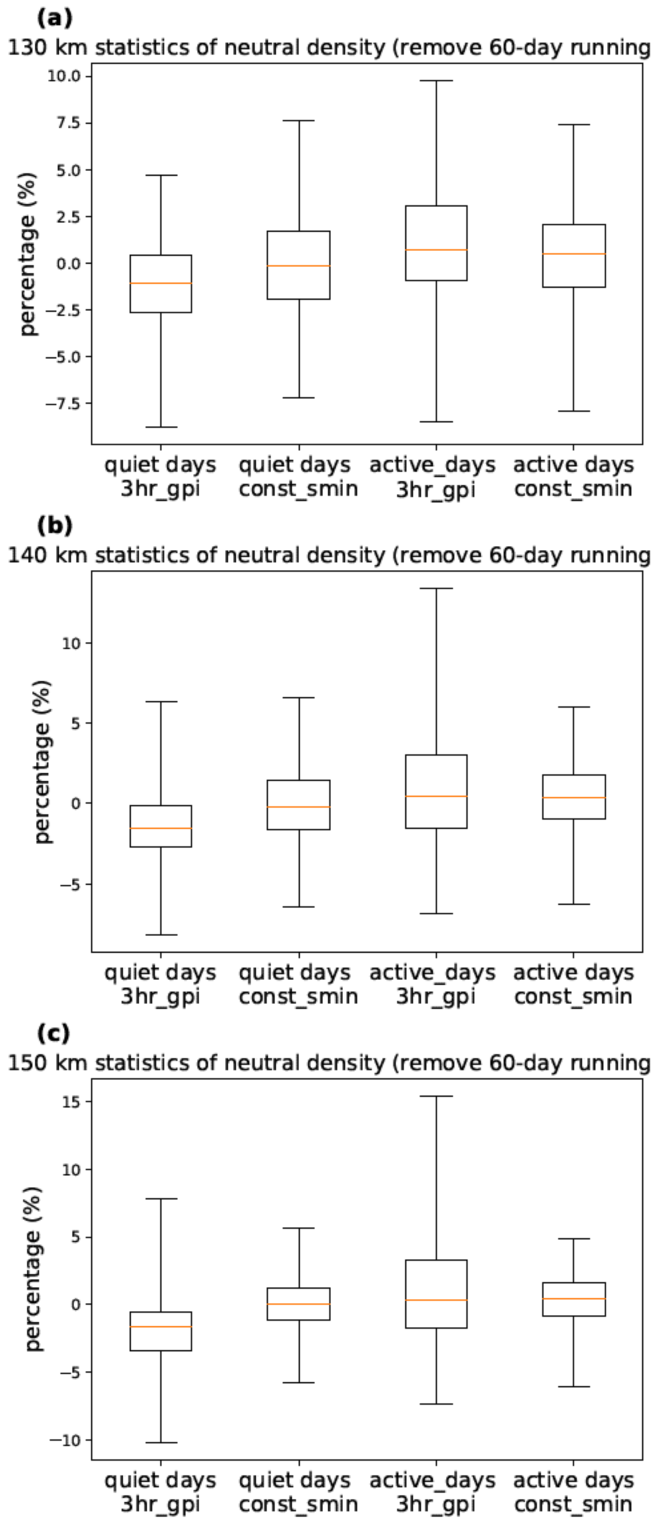

Figure 11. Similar to Figure 5 at 130 km, 140 km, and 150 km.

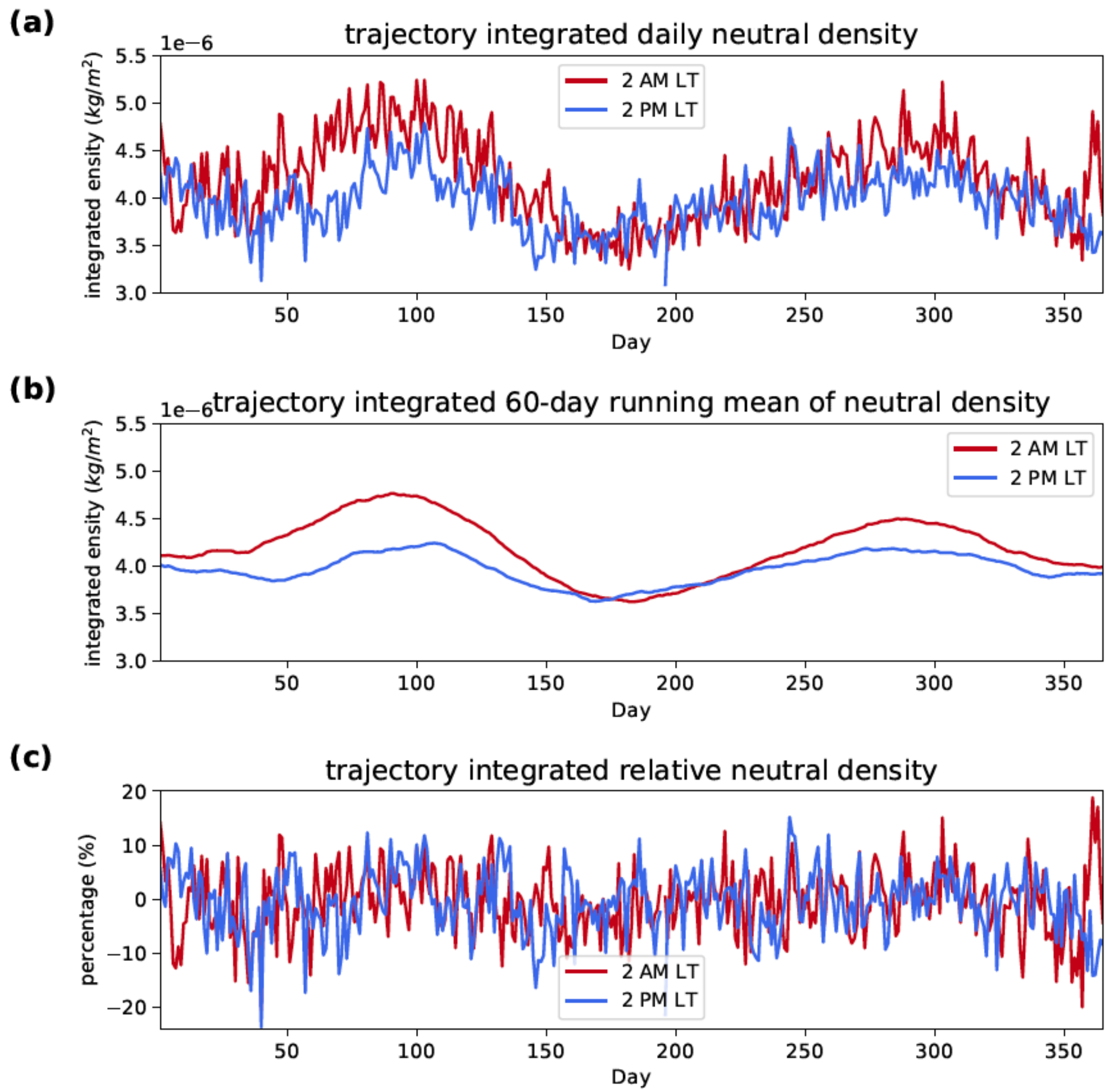

Figure A1. Similar to Figure 7, but along a more realistic vertical reentry trajectory.

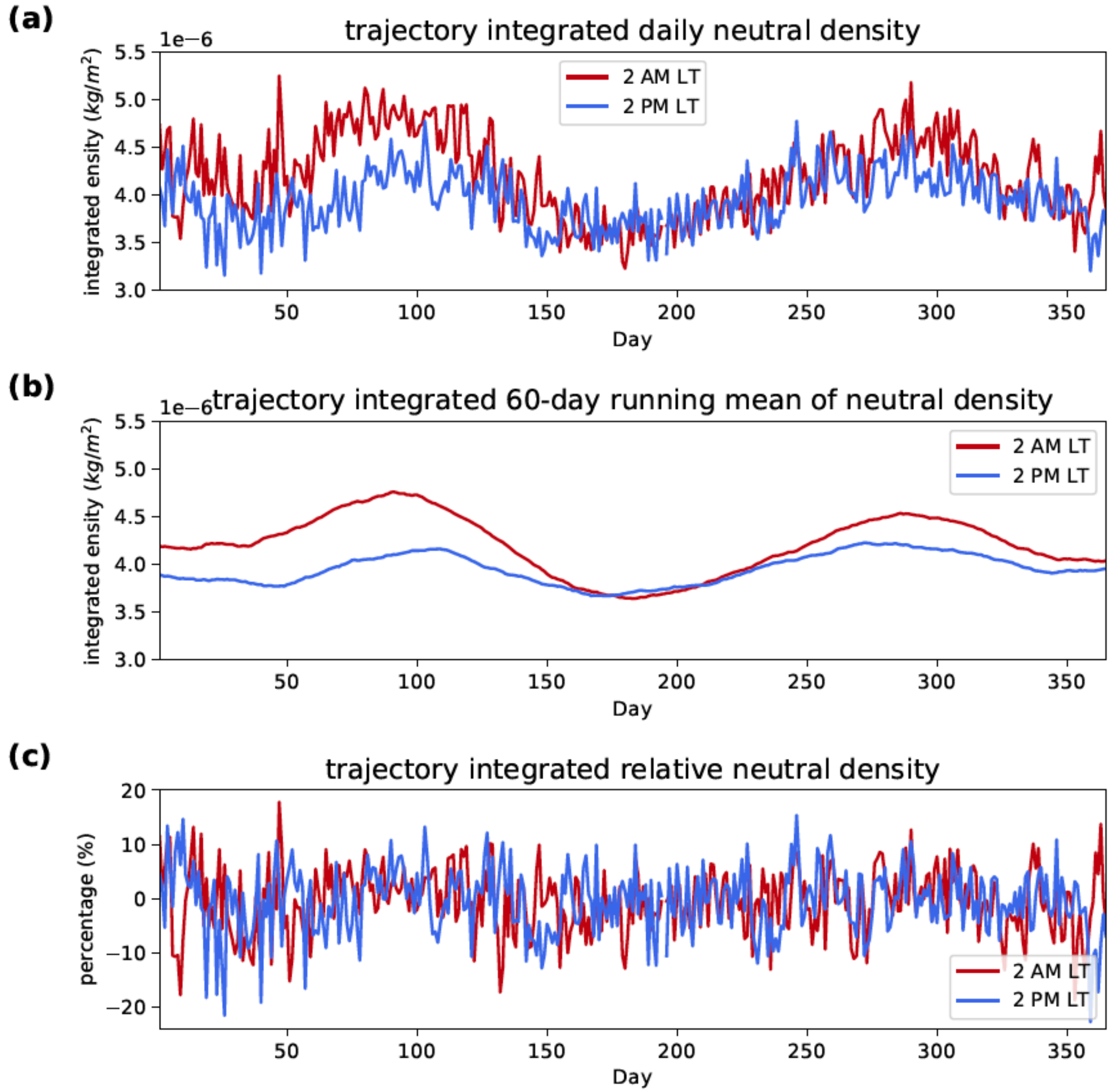

Figure A2. Similar to Figure 8 along a realistic reentry trajectory.

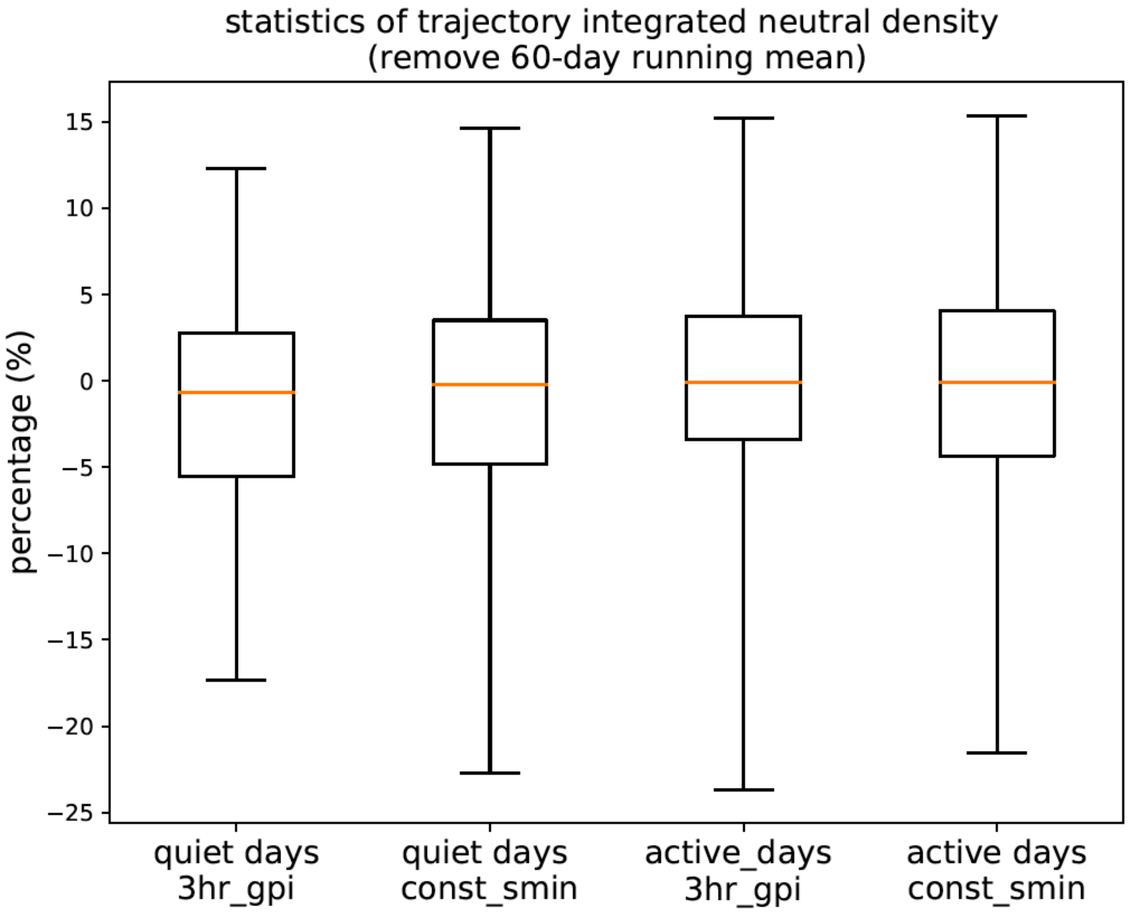

Figure A3. Similar to Figure 9, along a realistic reentry trajectory.

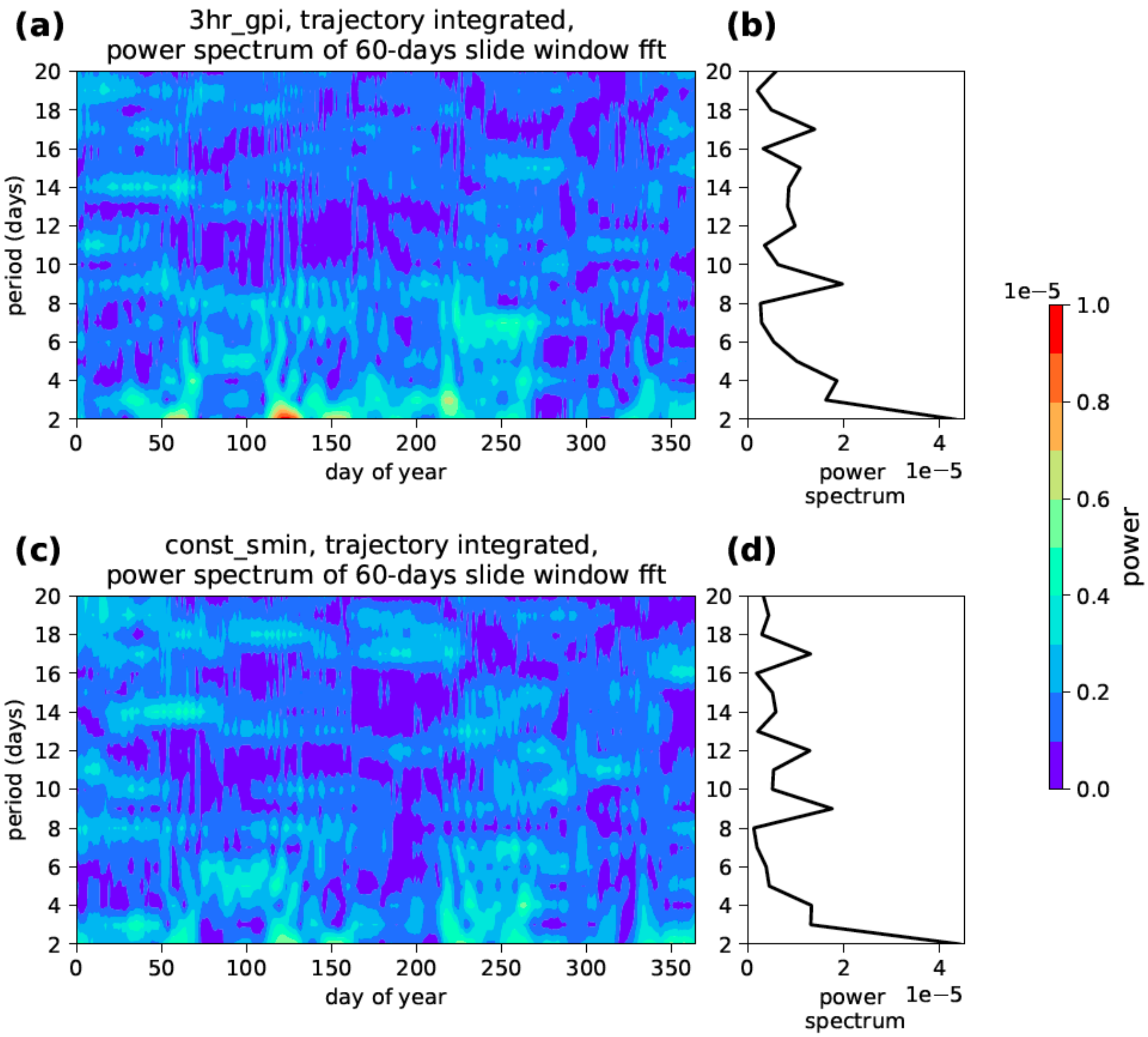

Figure A4. Similar to Figure 10, but along a realistic reentry trajectory.